Supplementary Material for

Surface plasmon delocalization in silver nanoparticle aggregates revealed by subdiffraction supercontinuum hot spots

Nicholas J. Borys[1] *, Eyal Shafran*[1]*, and John M. Lupton*[1,2]

[1]Department of Physics & Astronomy, The University of Utah, Salt Lake City, UT 84112, USA

[2]Institut für Experimentelle und Angewandte Physik, Universität Regensburg,

93053 Regensburg, Germany

I. Incident Excitation Power and Peak Intensities

The size of the illumination spot for all of the measurements that are presented in this work was ~75 μm in diameter. In general, incident powers were selected to maximize the signal-to-noise ratio and minimize any observed photo-modification effects. The lowest growth-time film necessitated the largest excitation powers, while the high coverage films required an excitation intensity that was smaller by nearly an order of magnitude. For the excitation spectroscopy measurements, the intensities are reported for illumination at 1.77 eV (700 nm) and the intensities of the other energies were chosen in order to maintain a constant flux of incident photons.

Dataset	Equivalent c.w. Power (mW)	Approx. Peak Excitation Intensity (MW/cm^2)
Figure 1		
Growth time 255 s	5.0	10
Figure 2		
Growth time 45 s	40	80
Growth time 135 s	6.0	12
Growth time 255 s	5.0	10
Figure 3		
Growth time 45 s	40	80
Growth time 75 s	7.5	9.2
Growth time 105 s	7.5	9.2
Growth time 135 s	6.0	12
Growth time 165 s	6.0	12
Growth time 195 s	3.0	6.0
Growth time 225 s	5.0	10
Growth time 255 s	5.0	10
Figure 4		
Growth time 255 s	5.0	10
Figure S6		
Growth time 255 s	3.0	6.0

Supplementary Table S1 – Excitation densities reported in the equivalent c.w. power and approximate peak intensity that were used in the datasets presented in the main text.

II. Excitation Polarization Anisotropy Measurements

Due to the oblique incidence of the excitation illumination, the excitation polarization does not always lie entirely within the plane of the sample. To clarify the details of the measurement, Fig. S1 shows a schematic of the configuration used to illuminate the sample and illustrates how the orientation of the polarization modifies the amount of excitation that is *parallel* and *normal* to the sample plane. As illustrated in panel (a), two important planes and their respective coordinate systems (where the *x*-axis is the horizontal direction and the *y*-axis is the vertical direction in the respective planes) should be considered in this configuration. The first is the sample plane or "*s*-plane" which contains the nanostructured silver film. Second is the "*k*-plane" which is defined as the plane that is normal to the propagation direction (i.e., the **k** vector) of the incident excitation laser light. Although the excitation illumination is focused on the sample, the electric field of the excitation laser is assumed to be primarily parallel to the *k*-plane for all of the laser polarization orientations at the sample surface.

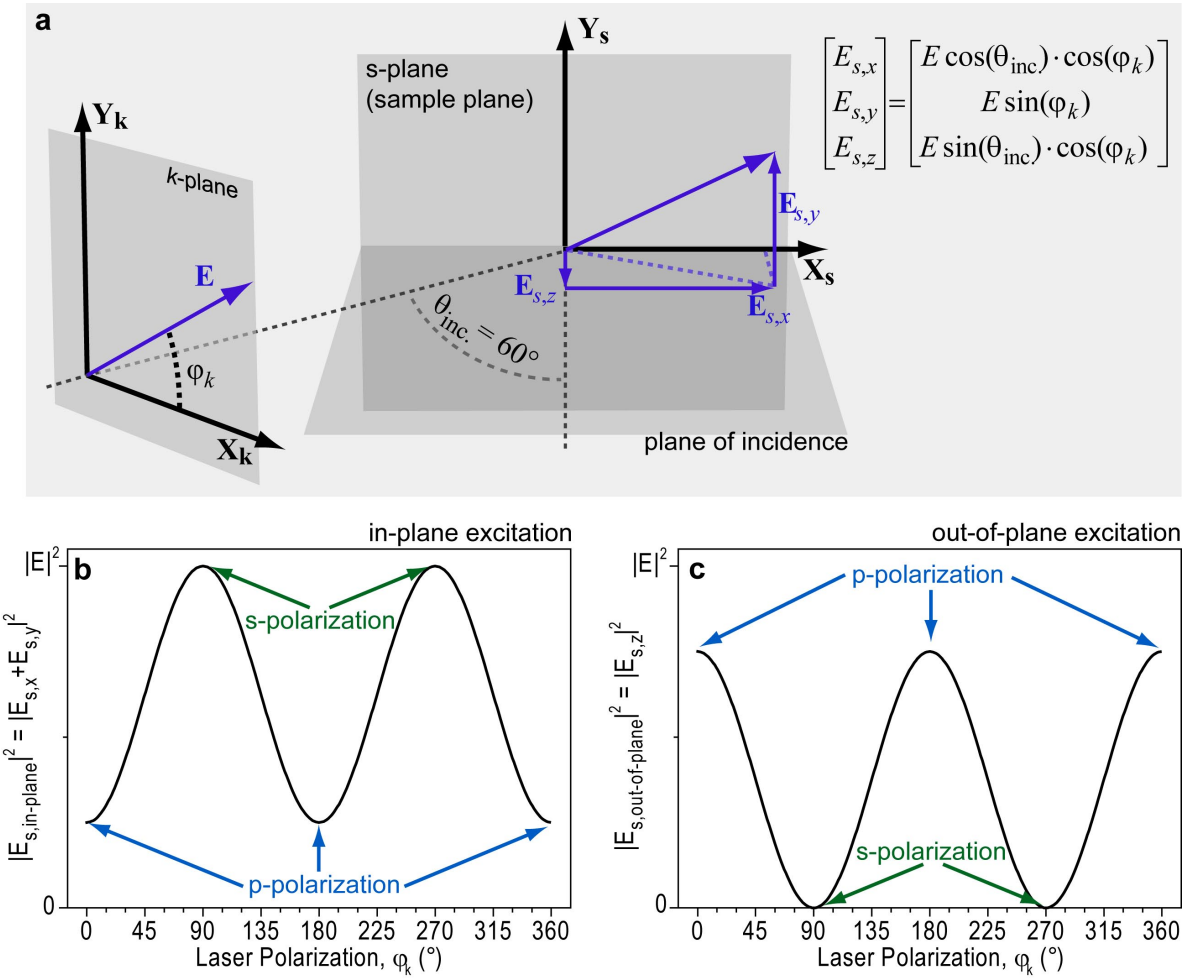

Supplementary Figure S1 – Detailed schematic of the excitation configuration and the orientations of the electric field of the linearly polarized excitation with respect to the plane of the sample. (a) The excitation light is linearly polarized and the electric field lies entirely within the plane that is orthogonal to the propagation direction of the light, the *k*-plane, which is oriented at a 60° angle with respect to the plane of the sample, the *s*-plane. Thus, the polarization angle of the laser in the *k*-plane changes the magnitude of the excitation that is polarized in the plane of the sample (b) and normal to the plane of the sample (c). When the laser is polarized vertically, or *s*-polarized ($\varphi_k = 90°, 270°$), the electric field that is parallel to the sample plane is maximized, thus maximizing the in-plane excitation. On the other hand, when the laser is polarized horizontally, or *p*-polarized ($\varphi_k = 0°, 180°, 360°$), the normal component and, consequently, the out-of-plane excitation is maximized.

At the oblique angle of incidence, $\theta_{inc} = 60°$, the two planes are not parallel. A counter-clockwise rotation of the *k*-plane by θ_{inc} about its *y*-axis is required to align the two planes and their respective coordinate systems. This rotation can be used to derive the expression for the components of the electric field vector of the laser in the coordinate system of the *s*-plane, $\mathbf{E}_{laser,s}$, as a function of the orientation of the laser's polarization in the *k*-plane, which is described by the angle φ_k:

$$\mathbf{E}_{laser,s} = \begin{bmatrix} E_{s,x} \\ E_{s,y} \\ E_{s,z} \end{bmatrix} = \begin{bmatrix} E\cos\theta_{inc}\cos\varphi_k \\ E\sin\varphi_k \\ E\sin\theta_{inc}\cos\varphi_k \end{bmatrix}. \quad (1)$$

The harmonic time dependence ($e^{i\omega t}$) has been omitted for the sake of clarity. From Eq. (1), it is evident that the excitation fields that are polarized *parallel* (Fig. S1(b)) and *normal* (Fig. S1(c)) to the sample plane depend upon the polarization state of the laser. When the excitation illumination is *p*-polarized (i.e., when $\varphi_k = 0°$ and the electric field lies within the plane of incidence), the in-plane excitation intensity is minimized (Fig. S1(b)) while the out-of-plane excitation intensity is maximized (Fig. S1(c)). When the laser is *s*-polarized (i.e., when $\varphi_k = 90°$ and the electric field lies perpendicular to the plane of incidence), the in-plane excitation is maximized, and the out-of-plane excitation is minimized to zero.

A nonlinear excitation dipole moment that is oriented normal to the sample plane will only be excited by out-of-plane polarization. As shown in Fig. S1(c), the intensity of this out-of-plane excitation exhibits a $\cos^2$ dependence on the laser polarization angle with the maximum intensity occurring for $\varphi_k = 0°$. Thus, in the polarization anisotropy measurements that are shown in the main text, an excitation dipole with such a perpendicular orientation will produce a modulation curve with a $\cos^4$ (the 4th power arises from the nonlinear power dependence of the hot spot) dependence on φ_k with an angle of maximum hot spot emission intensity of 0°.

The case of a nonlinear excitation dipole that is oriented *in the sample plane* (i.e., parallel to the plane) is summarized in Fig. S2. A dipole that lies at an angle, α_s, with respect to the *x*-axis (i.e., the horizontal direction) in the sample plane will project a dipole in the *k*-plane with an angle, α_k. Since the electric field of the excitation light lies entirely within the *k*-plane, the component of the excitation dipole that is orthogonal to this plane can be disregarded. By performing a similar transformation, namely a *clockwise* rotation by θ_{inc} about the *y*-axis, the projection of the excitation dipole in the *k*-plane can be determined. The orientation of the projected dipole will make an angle with respect to the *x*-axis (again, the horizontal direction), α_k, that depends on the initial orientation *and* the angle of incidence:

$$\alpha_k = \tan^{-1}\left(\frac{\tan\alpha_s}{\cos\theta_{\text{inc}}}\right) \tag{2}$$

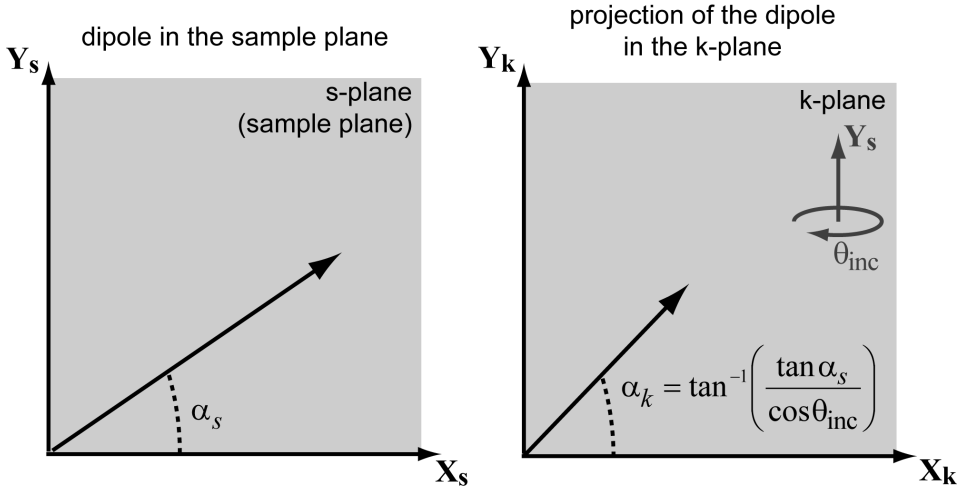

Supplementary Figure S2 – Projection of a dipole in the plane of the sample (the *s*-plane) into the *k*-plane. A dipole that lies within the sample plane with an angle, α_s, projects a dipole into the *k*-plane with a corresponding angle, α_k, which is determined by the orientation in the *s*-plane and the angle of incidence, θ_{inc}.

The dipole projected into the *k*-plane can then be treated with Malus's Law and related to the quantities from the excitation anisotropy measurements that are reported in the manuscript. Because the dipole is nonlinear, it will produce a modulation curve that follows a $\cos^4$ dependence on the laser polarization angle, φ_k, with an angle of maximum hot spot emission of $\varphi_k^{\max} = \alpha_k$. From this angle, the orientation of the dipole in the sample plane, $\varphi_{\text{dipole}} = \alpha_s$ can be extracted using Eq. (2):

$$\varphi_{\text{dipole}} = \tan^{-1}(\cos\theta_{\text{inc}} \cdot \tan\varphi_k^{\max}). \qquad (3)$$

III. Distributions of Excitation Dipole Angles for Random Dipole Orientations in Two and Three Dimensions

For comparison to the distributions of in-plane dipole orientations that are shown in Fig. 2 of the main text, the expected distributions of angles of maximum emission in the *k*-plane and the resulting dipole orientations in the *s*-plane as calculated with Eq. (3) for random orientations of dipoles in three-dimensions and two-dimensions are shown in Fig. S3. In each case, 10,000 dipoles with equal magnitude were generated numerically with random orientations. Using an angle of incidence of 60°, a simulated modulation curve was extracted and fitted to a $\cos^4$ function from which the angle of maximum emission was computed and then converted to a corresponding in-plane dipole angle using Eq. (3). As expected, both distributions produce anisotropy values (*M*) of unity as seen in Figs. S3(a) and S3(d). The slight deviations from unity reflect the numerical error that is introduced in the fitting routine. The 2D distribution of dipole orientations produces a distribution of *k*-plane angles (Fig. S3(b)) exhibiting a peak that is centred around the *s*-polarized excitation at -90° and 90°. By converting the *k*-plane angles into the in-plane dipole angles using Eq. (3), the uniform distribution of dipole orientations within the sample plane is recovered as shown in Fig. S3(c). In contrast, the 3D distribution of dipoles produces a flat distribution of angles of maximum emission in the *k*-plane (Fig. S3(e)) and a broadly peaked distribution of angles in the *s*-plane (Fig. S3(f)).

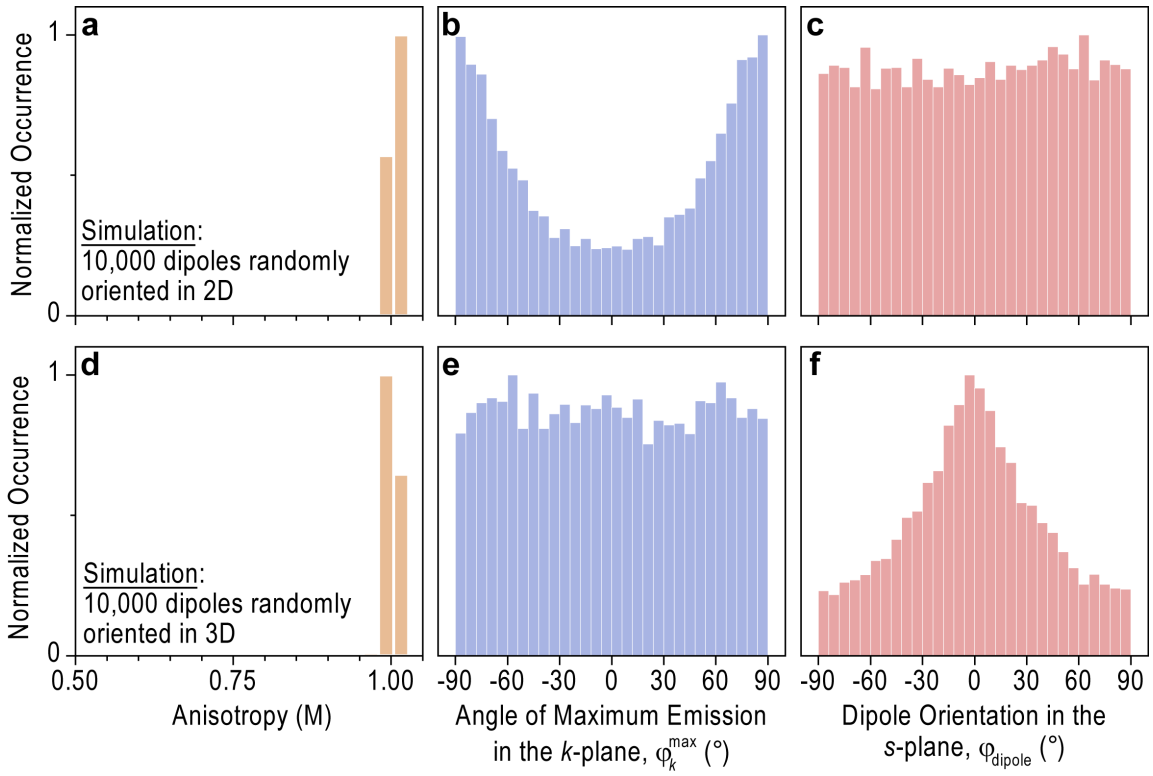

Supplementary Figure S3 – Example distributions for simulated polarization anisotropy measurements for a random set of dipole orientations in 3D and 2D. In 2D, the anisotropy (a) is always unity, while the distribution of dipole angles in the *k*-plane (b) shows pronounced peak-like features at the *s*-polarized states of the incident laser. By converting the angles to their corresponding dipole angle in the *s*-plane (c), the uniform distribution of dipole angles is obtained. In 3D, the anisotropy (d) is again unity, and the distribution of dipole angles measured in the *k*-plane (e) is uniform. Converting the *k*-plane angles into *s*-plane angles (f) produces a broadly peaked distribution at 0°.

The narrow peak centred on 0° in the measured distributions in Column 3 of the main text does not agree with either of these simulated distributions. The peak in the measured data is significantly narrower than the peak from the simulation for the 3D case (Fig. S3(f)). Furthermore, the peak in the measured data also appears in the corresponding distribution of angles of maximum emission ($\varphi_k^{\max}$) yet no peak is present in either of the simulations (Figs. S3(b) and S3(c)). We therefore conclude that the excitation dipoles of the silver films are either oriented parallel to the plane and produce a broad uniform distribution as shown in Fig. S3(c) or

are oriented perpendicular to the sample plane and produce a distribution with a sharp peak at 0° corresponding to *p*-polarized excitation.

IV. Distributions of Resonance Widths, Excitation Anisotropy Values and Dipole Orientations for all Values of Surface Coverage

Figure S4 shows the complete set of distributions of resonance widths, excitation anisotropy values, and dipole orientation angles that were used to calculate the data points in Figs. 3(b), 3(c), and 3(d), respectively. The trends that are summarized in Fig. 3 for each value are identifiable by eye. The centres of the distributions of resonance widths in Column A show a nearly monotonic decrease in value with increasing surface coverage. Likewise, the population of less-polarized hot spots in Column A that is described by a broad Gaussian distribution in Row I (growth-time 45 s) disappears in a step-like manner in Row IV. To perform the bimodal fitting that was required for the data points in Fig. 3(c) on Rows IV – VIII where the less-polarized distribution disappears, the centre and width of the lower-valued Gaussian peak were fixed to values of 0.65 and 0.4, respectively and only the amplitude was fitted. These values were taken as the average values from the fits to the anisotropy distributions in Rows I-III. Finally, in Column C, the distribution of dipole angles in the sample plane shows a similar step-like reduction in the number of in-plane excitation dipoles and consists of only a narrow peak at 0° for Rows IV – VIII.

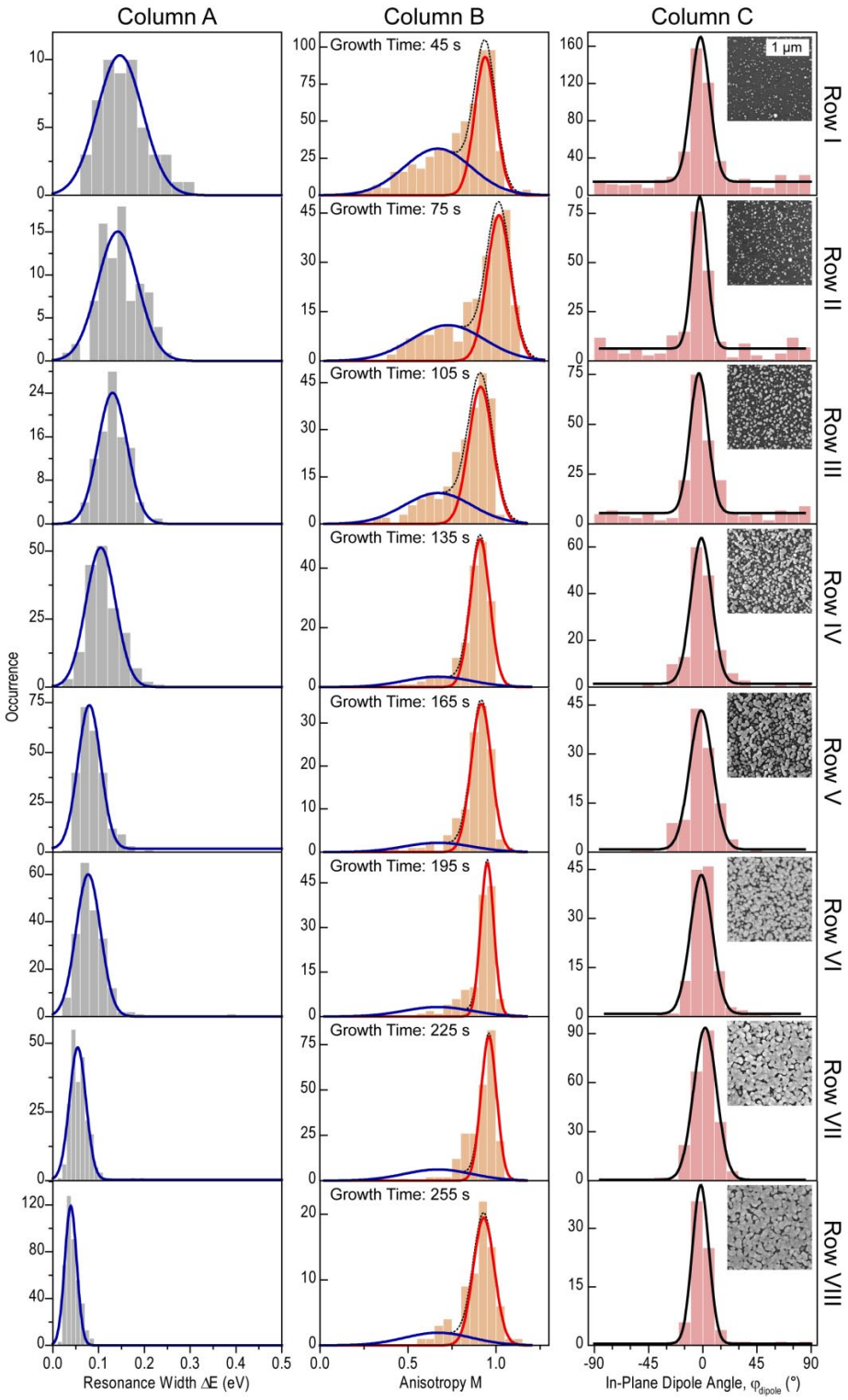

Supplementary Figure S4 – Resonance widths, excitation anisotropy values, and dipole orientation angles of the nonlinear hot spots for all growth times that are reported in Figure 3 of the manuscript.

V. Calculation of 2D Filling Factors

Figure S5 illustrates the process that was used to approximate the surface coverage of the nanostructured silver films with the 2D filling factor. Grayscale SEM images (Fig. S5(a)) were acquired of the silver films at a magnification of 60,000 (FEI Nova NanoSEM 630; Helix detector; 4.9 mm working distance; ~7 keV landing energy; 0.23 nA beam current). These images were binarized (i.e., converted to black and white) using ImageJ where pixels that were brighter than a threshold value were converted to white and those that were dimmer to black (Fig. S5(b)). For each greyscale image, the threshold value was selected with the aid of the distribution of pixel intensities (Fig. S5(a) inset) such that the shape of the majority of silver regions was maintained as verified by manual comparison of the resulting binary image with the original greyscale image. Finally, the filling factor was approximated by the relative number of white pixels:

$$\text{Filling Factor} = \frac{\text{White Pixels}}{\text{Total Pixels}} \tag{4}$$

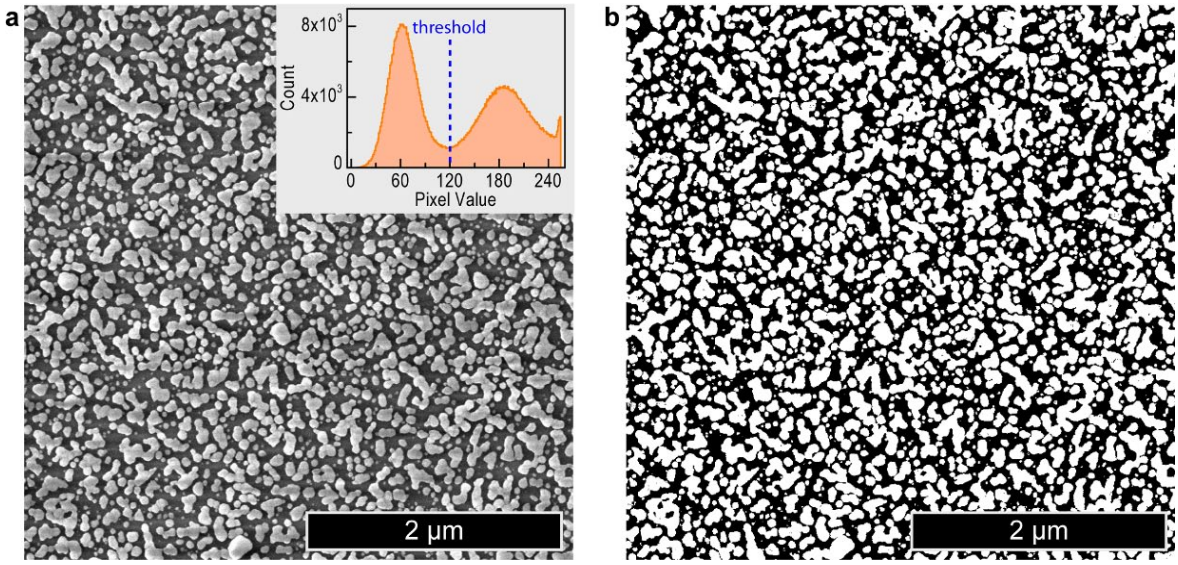

Supplementary Figure S5 – Two-dimensional filling factor calculation. Panel (a) shows an SEM image of a silver film along with the distribution of pixel intensities. Using the distribution as a guide, the pixels can be divided into bright and dark pixels where the bright pixels correspond to silver. In panel (b), the greyscale SEM image is converted to a binary image where the pixels above the threshold value are converted to white while those below the threshold value are converted to black. Comparison of the two images in panel (a) and (b) provides qualitative assurance that the threshold value accurately divides the pixels into silver and non-silver regions. Finally, the filling factor can be calculated by the fraction of bright pixels in the image.

VI. Emission Spectroscopy of Multi-Resonant Hot Spots

We measured the *emission* spectrum of a single hot spot at each of its *excitation* resonances for several individual hot spots. A representative hot spot from a semicontinuous film (growth time 255 s) is shown in Fig. S6. As seen in Fig. S6(a), the hot spot exhibits three distinct resonances at energies of 1.71 eV, 1.64 eV, and 1.58 eV. By isolating the single hot spot with the slit in the imaging spectrometer and introducing a grating to spectrally disperse the light, we are able to record the emission spectrum of the single hot spot. Panels (b)-(d) show emission spectra of the hot spot at each of its three resonances. The narrow resonances of the hot spot produce broad emission, yet, compared to the variation *between* hot spots [S1], the emission spectrum shows virtually no change across the three resonances. Thus, the different excitation resonances of the single hot spot produce nearly identical emission, suggesting that the emission does indeed arise from the same species on the sample.

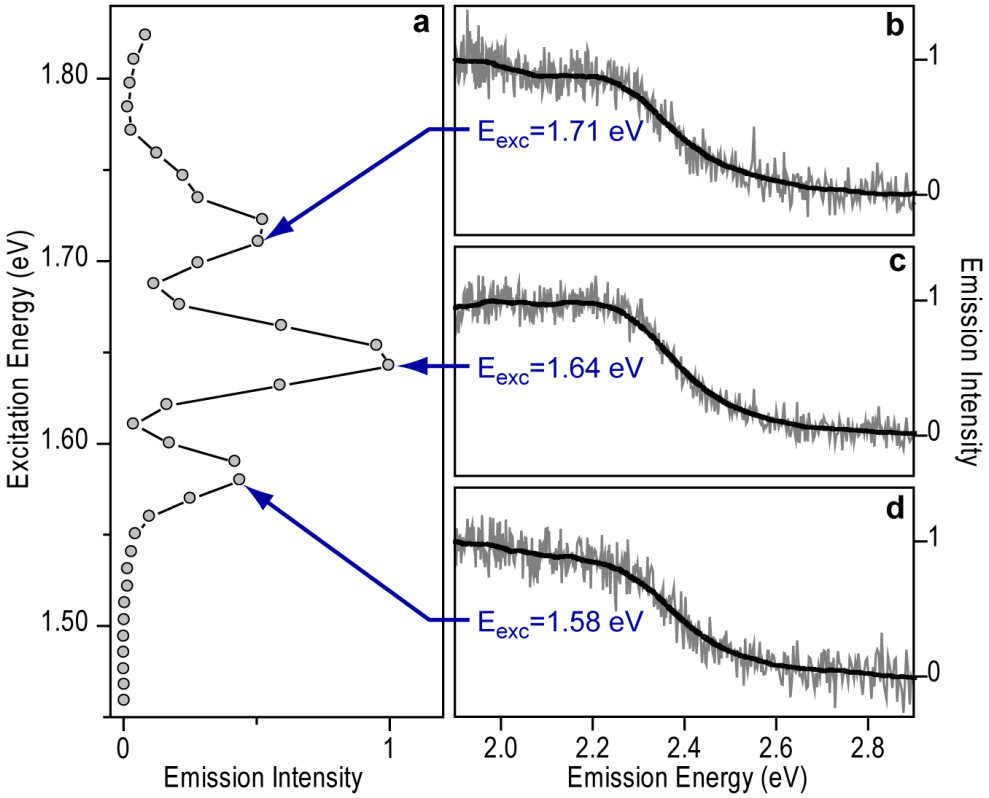

Supplementary Figure S6 – Emission spectra of a single, multi-resonant nonlinear hot spot. (a) The excitation spectrum reveals three distinct resonances. (b)-(d) Corresponding emission spectra of the different resonances. These spectra show very little variation, suggesting that the resonances are common to a single hot spot.

VII. Photon Localization Measurements of Multi-Resonant Hot Spots

The semicontinuous nanostructured silver film that was used for the localization measurements shown in Fig. 4 was prepared as described in the main text with a growth time of 255 s. After preparation, a water solution of latex beads (1.0 μm diameter; fluorescent yellow-green; Sigma Aldrich L4655) was diluted by a factor of 200:3. 50 μl of the diluted solution was placed on top of the Tollens film for approximately 45 min. allowing the beads to stick to the surface. After the deposition process, the remaining solution was blown off under a gentle stream of nitrogen. This deposition process yielded approximately 10 isolated beads per 50 × 50 μm area on the sample. The larger bead diameters were initially chosen to maximize their contrast in electron microscopy measurements. In order to utilize the beads to remove the effects of unwanted random stage motion during the course of the measurement, the sample was collinearly illuminated with IR excitation to excite the nonlinear hot spots along with a very weak (~1 μW) c.w. visible excitation at 458 nm (Coherent Innova Ar+). Due to the very low incident power, the silver films did not show any observable optical response under illumination at 458 nm alone. Rather, this laser only excited fluorescence from the beads that provided registration points allowing any random motion of the sample to be tracked and removed in the final data analysis.

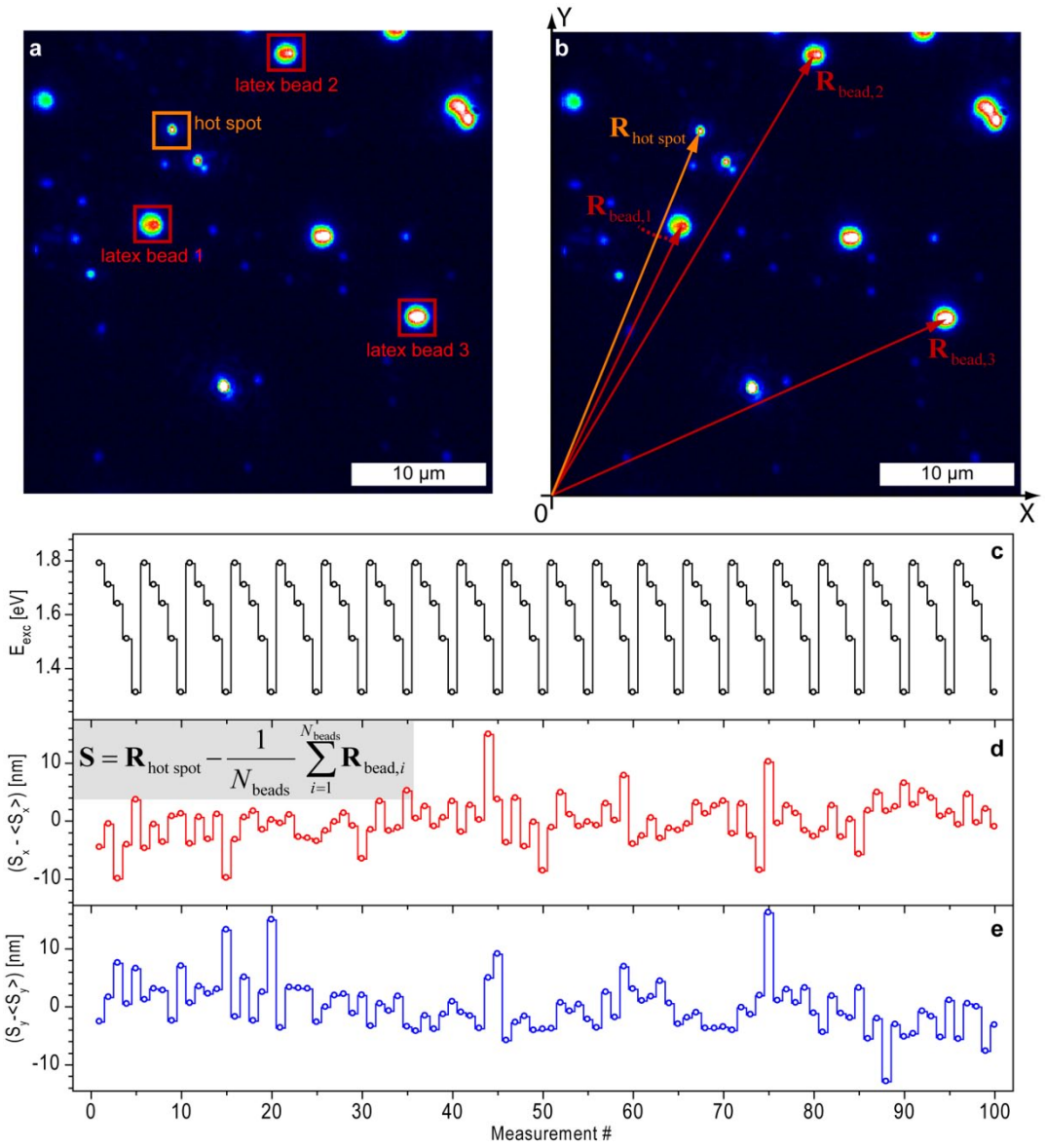

Supplementary Figure S7 – Localization microscopy measurement of the multi-resonant hot spot from Fig. 5(b) with resonances at 1.79, 1.71, 1.64, 1.51 and 1.31 eV. Shown in panel (a) is a fluorescence micrograph of a Tollens film (growth time 255 s) with 1 µm diameter fluorescence beads. In (b), the image coordinates of the beads and hot spot are determined by fitting a 2D Gaussian to each emission profile. In each measurement step, the excitation energy is set to one of the resonances of the hot spot and each resonance is probed 20 times as shown in (c). By subtracting the average of the bead positions to obtain the quantity **S**, the average shift in centroid position, the thermal drift of the microscope can be removed, and the relative change of the hot spot position at each resonance can be recorded for the *x* and *y*-directions as shown in panels (d) and (e), respectively.

An optical micrograph of the fluorescence from the beads in conjunction with the nonlinear emission from the nanostructured silver film is shown in Fig. S7(a). The beads are easily discernible from the hot spots, as they only produce detectable emission when illuminated with the 458 nm laser. A nonlinear excitation measurement was first conducted to identify the resonances of the single nonlinear hot spots (c.f. Fig. 4(b)). For the hot spots that appeared spatially isolated, optical micrographs of the hot spot and fluorescent beads were sequentially acquired 20 times at each of the specific resonant energies. An example of one such micrograph and the alternating excitation scheme are shown in Figs. S7(b) and S7(c), respectively. At each excitation energy, the emission profiles of the hot spots and beads were fitted to a 2D Gaussian and the respective centroid positions, $\mathbf{R}_{\text{hot spot}}$ and $\mathbf{R}_{\text{bead},i}$, were extracted. The "trajectory" of the hot spot was then recorded over the course of the measurement and corrected for stage movements by subtracting the average centroid position of the beads from the position of the hot spot to obtain the quantity **S**:

$$\mathbf{S} = \mathbf{R}_{\text{hot spot}} - \frac{1}{N_{\text{beads}}} \sum_{i=1}^{N_{\text{beads}}} \mathbf{R}_{\text{bead},i} \qquad (5)$$

Since the motion of the beads does not vary with changing IR excitation energy, the quantity **S** is invariant with respect to random stage motion and drift leaving only centroid shifts of the hot spot that are induced by changing the IR excitation energy. The removal of the stage motion can be seen in Figs. S7(d) and S7(e), where the deviations of S_x and S_y from their average values are tightly grouped around 0 nm for the hot spot shown in Fig. S7(b). Using multiple beads served to reduce errors in the approximation of the stage movements, and beads that showed any indication of significant photo-bleaching or a gradual change in their spatial emission profile were discarded.

The inter-resonance shifts of the hot spot's emission centroid were calculated as the difference between consecutive values of **S** that were obtained at different excitation energies. For example, the hot spot in Fig. S7 with 5 resonances, E_1, E_2, E_3, E_4, and E_5, has 10 possible inter-resonance shifts:

$$\begin{aligned}
\Delta r_1 &= \Delta r_{E_1-E_2} = \frac{1}{20}\left|\sum_{i=0}^{19}(\mathbf{S}_{5i+1}-\mathbf{S}_{5i+2})\right| \\
\Delta r_2 &= \Delta r_{E_1-E_3} = \frac{1}{20}\left|\sum_{i=0}^{19}(\mathbf{S}_{5i+1}-\mathbf{S}_{5i+3})\right| \\
&\cdots \\
\Delta r_{10} &= \Delta r_{E_4-E_5} = \frac{1}{20}\left|\sum_{i=0}^{19}(\mathbf{S}_{5i+4}-\mathbf{S}_{5i+5})\right|.
\end{aligned} \tag{6}$$

To determine the spatial resolution of the measurement, the process described was applied to individual beads in place of hot spots where the quantity **S** should not show any movement. The resulting localization of several beads is shown in Fig. S8. As can be seen from the distributions, the emission centroids of individual beads can be localized to the same region over the course of such a measurement (~20 minutes) with an accuracy of ~2 nm and ~4 nm in the *x* and *y* directions, respectively.

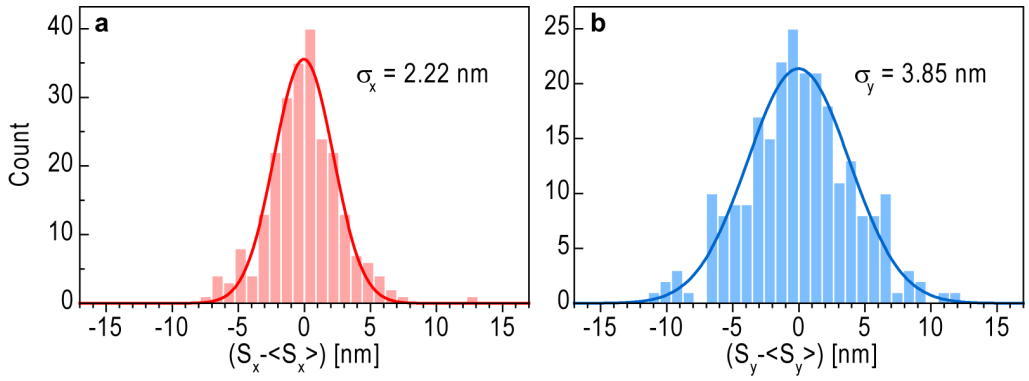

Supplementary Figure S8 – Resolution of the localization measurement. By applying the procedure summarized in Fig. S6 (plus Eqs. S5 and S6) to each bead with respect to the other beads, the resolution of the localization measurement can be estimated. In the *x*-direction (a), the beads are localized to the same position with a standard deviation of ~2 nm, while in the *y*-direction (b), the beads are localized to the same position with a standard deviation of ~4 nm.

VIII. References

[S1] Borys, N. J. & Lupton, J. M. Surface-enhanced light emission from single hot spots in Tollens reaction silver nanoparticle films: Linear versus nonlinear optical excitation. *J. Phys. Chem. C* **115,** 13645–13659 (2011).